Structure and Properties of Synoptic-Scale Wave Disturbances in the Equatorial Western Pacific

RICHARD J. REED AND ERNEST E. RECKER

Dept. of Atmospheric Sciences, University of Washington, Seattle

(Manuscript received 8 March 1971, in revised form 7 June 1971)

ABSTRACT

A compositing technique is used to obtain the average structure of 18 disturbances which traversed an area in the equatorial western Pacific during the wet season (July–September) of 1967. Principal emphasis is placed on the wave properties in the triangular area described by Ponape, Kwajalein and Eniwetok within which it was possible to measure divergence and vertical motion and to compute moisture and heat budgets.

Meridional wind maxima of nearly opposite phase occurred in the lower and upper troposphere. Negative temperature deviations were found in the vicinity of the wave trough at low and high levels; positive deviations were observed at intermediate levels. Highest relative humidities occurred in the trough region. This was also the region of strongest upward motion and greatest rainfall and cloud amount. The maximum upward velocity of 2.5 cm sec^{-1} was found at 300 mb. Convergence was strongest in the sub-cloud layer; divergence was concentrated near 175 mb. The maximum anticyclonic vorticity was also observed at that level.

The wave structure changed in a systematic fashion across the network. The change is attributed to the variation with longitude of the shear of the basic current.

The rainfall computed from the observed wind and moisture fields agreed well with observed amounts which varied from about 2 cm day^{-1} in the vicinity of the trough axis to about 0.5 cm day^{-1} near the ridge axis. The diabatic heating difference between trough and ridge regions was largest at 400 mb where it was estimated to be nearly 10C day^{-1}.

1. Introduction

The existence of westward traveling wave disturbances in the trade wind easterlies and the easterlies of the equatorial trough region, or Intertropical Convergence Zone (ITCZ), has been recognized since the early studies of Riehl (1945) and Palmer (1952). The structure and properties of these systems have been examined in a number of ways. Case studies have been made of individual systems utilizing ordinary synoptic methods (Riehl, 1945, 1965; Yanai, 1961, 1963, 1968). Spectrum and cross-spectrum analysis have been employed to obtain objective descriptions of their characteristics (Yanai *et al.*, 1968; Wallace and Chang, 1969; Nitta, 1970; Chang *et al.*, 1970; Wallace, 1971). A compositing technique developed by Williams (1970) has yielded valuable information concerning their average properties. Studies utilizing satellite photographs have revealed characteristic cloud patterns which allow the disturbances to be identified and tracked over long distances (Frank, 1969; Chang, 1970). Diagnostic studies, based on the hydrodynamic equations, have been used to infer parameters that cannot be directly measured and to obtain dynamically consistent pictures of the wave structure (Krishnamurti and Baumhefner, 1966; Yanai and Nitta, 1967; Holton, 1971).

Despite the progress that has been made in defining the structure of tropical disturbances, further studies are required. These are needed to extend and confirm the results of previous studies and particularly to examine seasonal and regional differences in behavior which must be understood before sound progress can be made in modeling the disturbances.

The purposes of the present study are 1) to define the structure of the westward propagating synoptic disturbances which were observed in the ITCZ of the equatorial western Pacific during the wet season (July–September) of 1967, and 2) to determine their heat and moisture budgets. The area considered and the observing network are shown in Fig. 1. The study is based

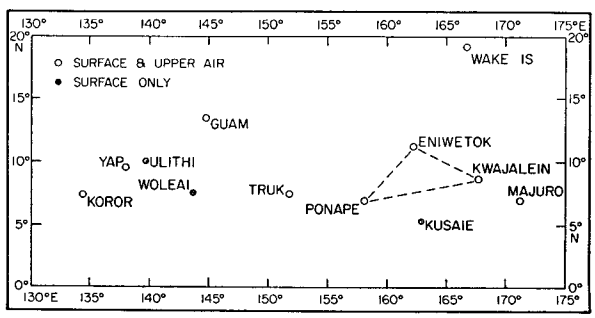

FIG. 1. Observational network in the equatorial western Pacific.

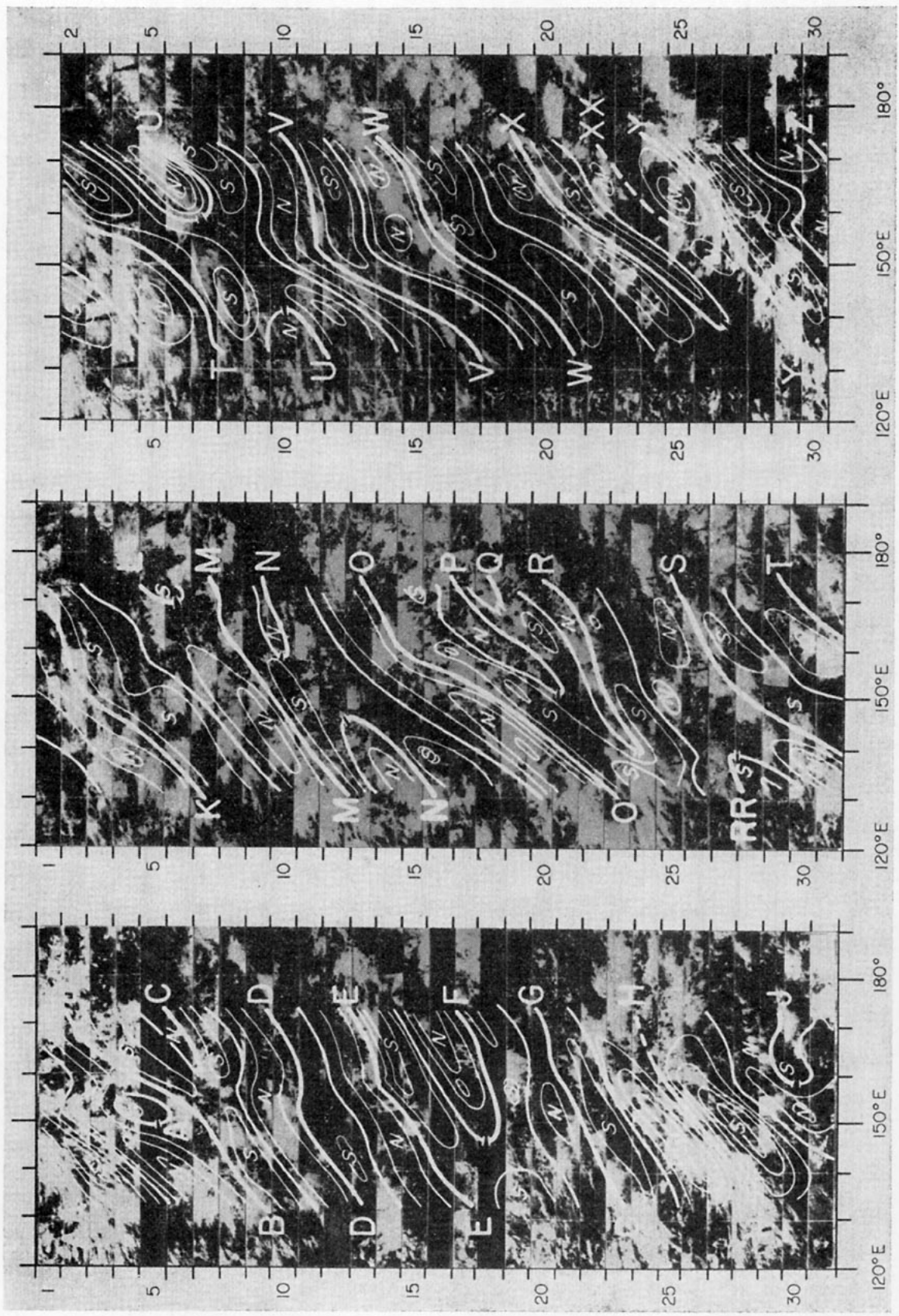

FIG. 2. Time-longitude sections for July, August and September (left to right) of the mean meridional wind in the layer from the surface to 500 mb superimposed on digitized satellite cloud mosaics. Isopleths are drawn at interval of 2 m sec^{-1}. Dates refer to local time.

on a compositing technique which gives average properties of the 18 disturbances which affected the area during the three-month period. Most of the disturbances could be classified as weak, though four were associated at some stage in their histories with tropical depressions or tropical storms. Two of the storms later developed into typhoons. All depressions and storms were centered well north of the network (15N or higher), and in only one case was there a long association between the equatorial wave and the related tropical storm. The main emphasis is placed on results from a triangle of stations (Kwajalein, Eniwetok and Ponape) for which it was possible to obtain divergences and vorticities in addition to the directly reported meteorological variables. The strongest surface winds observed at these stations during the three-month period were in the range 25–30 kt.

2. Method of analysis

The compositing was accomplished in the following manner. The vertically averaged meridional wind component for the layer from the surface to 500 mb was computed for each station at each synoptic observation hour. Before averaging in the vertical, the time series at each level were smoothed with a broad band-pass filter which effectively eliminated variations with periods less than 2 and greater than 15 days. The mean meridional winds obtained by this procedure for the seven upper air stations in the zone 7–11N were plotted on time-longitude sections and isotachs were drawn (Fig. 2). From the analysis it is possible to identify the separate waves and to trace their westward progression with time. The isopleths of zero meridional velocity denote the trough and ridge axes of the waves. The vorticity measurements presented in Section 4 support the use of the zero isopleths to define these axes.

Each trough line has been identified and labeled in a manner believed to be consistent with the data. Clearly the wavelength of the disturbances fluctuates greatly and not all waves can be traced across the entire network. Some waves are believed to have partly dissipated in the eastern area and then re-intensified and become discernible again near the western end of the network. Speed of propagation also varies substantially for different waves and for different longitudes.

Superimposed on the wind analyses are photographic strips for the belt between 5 and 10N constructed from daily digitized satellite mosaics from ESSA 5 in the manner described by Chang (1970). The mosaics were supplied on microfilm by the National Climatic Center. The winds were analyzed independently of the satellite data. It is evident, however, that the wind and cloud patterns are closely related.

The wind analyses in Fig. 2 were used to assign each observation for each station to one of eight categories denoted by the numerals 1 to 8. Categories 2, 4, 6 and 8 are centered, respectively, on the maximum northerly wind, the trough axis, the maximum southerly wind, and the ridge axis of the waves. Categories 1, 3, 5 and 7 occupy intermediate positions. The average values of the variables calculated for each category are used to define the typical wave structure. About 24 observations are contained in each mean.

On the cross sections depicting wave structure the horizontal coordinate is labeled in accordance with the wave features used to denote the categories. Since about 18 waves passed the stations during the three-month period, an average of one every five days, the abscissa can alternatively be regarded as a time axis with an interval of five days between successive ridge positions. Or, since the average wave speed was 7° of longitude per day, it can also be regarded as an east-west axis with an interval of 3800 km between successive ridge positions. The latter interpretation is permissible only to the extent that the waves maintained a steady state.

Horizontal divergence and the vertical component of vorticity were computed for the defined triangular area using the well-known method introduced by Bellamy. A linear correction was applied to the measured divergences for each synoptic hour in order to achieve mass balance in the layer from the surface to 80 mb. Even without this adjustment, it was found that approximate balance was attained in most categories in the three-month average. The vertical velocity ω in pressure coordinates was computed from the adjusted divergences by integration of the continuity equation with the boundary condition $\omega=0$ at the surface. The wave chronology for 163E was used in assigning categories to the triangle of observations.

The compositing technique was also applied to precipitation and opaque cloud cover amounts. Precipitation was totaled and opaque cloud cover amounts were averaged for 12-hr periods centered on 0000 and 1200 GMT, thus making these variables compatible in time with the radiosonde observations. For the three stations not having upper air observations (Kusaie, Woleai and Ulithi) appropriate chronologies extracted from the analysis in Fig. 2 were used.

Because of the substantial instrumental error that can occur in daytime humidity measurements (Morrissey and Brousaides, 1970; Colton, 1970), only nighttime values were used in this study.

3. Mean zonal wind

From theoretical reasoning (Riehl, 1954) and results of numerical modeling (Holton, 1971), it is apparent that the wave structure will be sensitive to the vertical profile of the basic current in which the wave is embedded. It is appropriate, therefore, to take note of the mean zonal current which prevailed over the area of study during the period July–September 1967. This

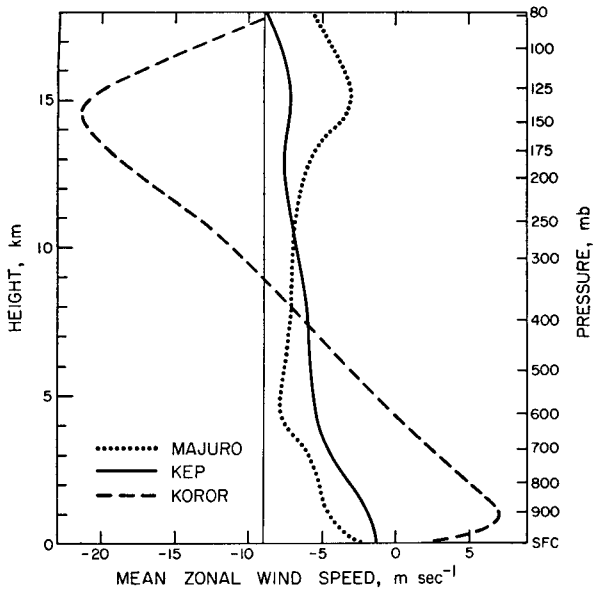

FIG. 3. Mean zonal wind speed for the period July–September 1967. The profile labeled KEP is the mean for Kwajalein, Eniwetok and Ponape. The thin vertical line denotes the average wave speed (-9 m sec^{-1}) observed during the period of study.

is shown in Fig. 3 for stations at the eastern and western ends of the network (Majuro and Koror) and for the triangle of stations, hereafter referred to as KEP, situated near, but somewhat to the east of, the center of the network. The figure reveals marked differences in wind profiles across the network, as was already known from climatological studies. The zonal wind component is easterly at all heights in the eastern end of the network with the highest speed occurring near 600 mb (5 km). At the western extremity the wind is westerly below 600 mb and easterly above. Very strong easterlies are observed in the upper troposphere. These are connected with the circulation about the upper level anticyclone which prevails over Southern Asia during summer.

Since the wave disturbances propagate westward at a speed of about 9 m sec^{-1} in the eastern half of the region, the mean air flow relative to the waves is westerly (from west to east) at all levels. The disturbances move westward at a somewhat slower speed in the western half. Here, on the average, the air enters the systems from the west below about the 400-mb level and from the east above.

4. Wave structure

The fields of the basic variables in the waves, derived from the compositing technique described in Section 2, will now be presented for the KEP triangle.

a. Meridional wind component

The major features revealed by Fig. 4 are the regions of maxima and minima in the lower and upper troposphere separated by a region of weak fluctuations near 300 mb. As required by the method of compositing, maximum northerly and southerly components in the lower troposphere lie midway between the trough and succeeding and following ridges, respectively. The maxima are located between 700 and 800 mb and slightly exceed 3 m sec^{-1} in magnitude. At lower levels the trough and ridge axes tilt eastward with height, the trough and ridge passages at the surface preceding those aloft by about one-tenth of a wavelength or one-half day.

The meridional wind fluctuations in the upper troposphere are nearly out of phase with those in the lower, the maximum south wind at high levels lagging the low-level northerly peak by approximately one-eighth of a wavelength. The upper level fluctuations are strongest in the layer 150–200 mb (12–15 km) where their amplitude reaches 2 m sec^{-1} or slightly greater.

b. Temperature

Because of the smallness of the temperature variations which occur with the passage of the wave, it is convenient to depict the temperature field (Fig. 5) in terms of deviations of the temperatures at the particular level from the mean value for the level. From the figure, it is seen that the amplitude of the deviations is a maximum at four levels. A first prominent maximum is found at the surface where a negative departure from the mean of nearly 0.5C is observed in the region immediately following the trough. Since, as will be shown later, the heaviest precipitation occurs in and somewhat ahead of the trough and since the air flow relative to the trough is from west to east (left to right in the

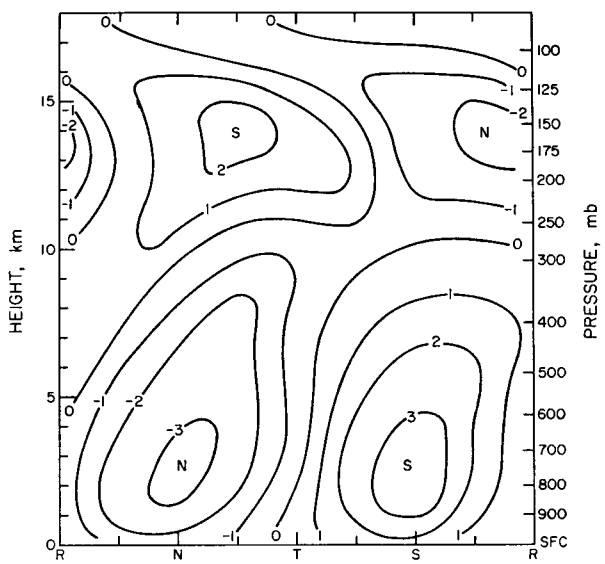

FIG. 4. Composite diagram of meridional wind speed (m sec^{-1}) for KEP. The letters R, N, T and S refer to the ridge, north wind, trough and south wind regions, respectively, of the wave as defined by its structure in the lower troposphere.

figure), it seems reasonable to ascribe the region of negative temperature anomaly to the cumulative effect of cooling in unsaturated downdrafts (Zipser, 1969). Cloud cover, which also is greatest in this part of the wave, probably contributes to the cool anomaly, but it cannot be its sole cause since the same pattern occurs at night.

A second but weaker level of maximum amplitude occurs near 700 mb. It, too, has coolest temperatures in the region just to the rear of the trough. Riehl (1969) has noted a similar feature in easterly waves and has suggested evaporative cooling as a possible cause. However, as will be shown subsequently, the temperature changes produced by vertical motions and associated release of latent heat are so large compared with the observed temperature fluctuations, which thus represent small residuals, that attempts to offer simple, qualitative explanations for the anomaly field near 700 mb, and elsewhere in the free atmosphere, do not seem warranted.

Other levels of maximum amplitude occur near 300 mb and in the region about 125 mb. The fluctuations at 300 mb are out of phase with those below, with warmest temperatures occurring just after the trough passage at low levels. The variations at the higher level are nearly in phase with those in the lower troposphere, exhibiting coldest temperatures above the low-level trough and warmest temperatures above the ridge.

Comparison of Figs. 4 and 5, regarding the abscissa as the east-west space coordinate, reveals that at most levels the thermal wind relationship is obeyed, at least qualitatively, and at some levels even quantitatively. For example, horizontal temperature gradients at 300 mb in some portions of the wave are of the order of 0.1C per one-tenth wavelength, or about 400 km, and

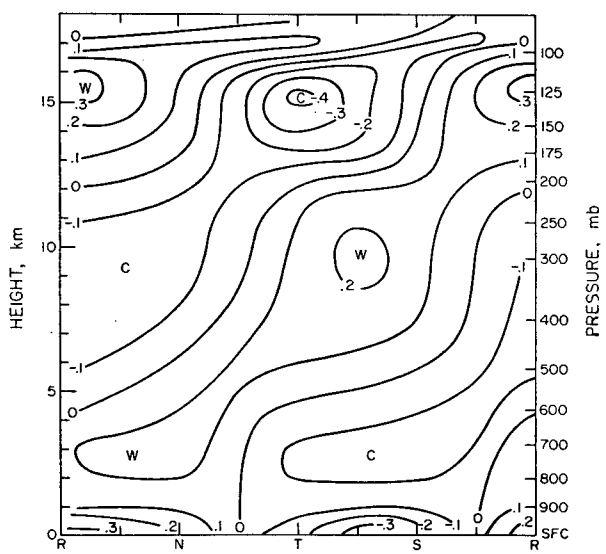

FIG. 5. Composite diagram of temperature deviations (°C) at various levels from their respective mean values at KEP. Refer to Fig. 4 for further explanation.

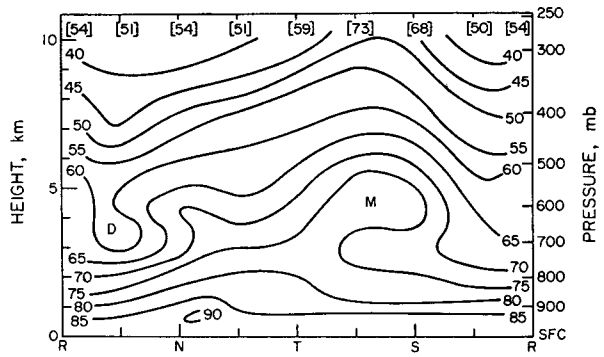

FIG. 6. Composite diagram of relative humidity for KEP. Values in brackets at the top are for saturation with respect to ice. Refer to Fig. 4 for further explanation.

corresponding vertical shears are 0.5–1 m sec^{-1} km^{-1}. For the inferred temperature gradient a shear of 0.5 m sec^{-1} km^{-1} constitutes perfect agreement with the thermal wind shear at the mean latitude of 9N. On the other hand, the quantitative agreement is poor in the region about 125 mb.

It should be noted that the virtual rather than the actual temperature deviation should be used when applying the thermal wind relationship. The virtual temperature is also required in other applications, such as in studying conversion from potential to kinetic energy where the product of the virtual temperature deviation and vertical velocity is required. Except at low levels the virtual temperature correction is small, and computations show that even at these levels the range of variation is not sufficient to alter the pattern of temperature deviation.

c. *Relative humidity*

The fluctuations are small below 800 mb (Fig. 6) and largest near 500 mb where values range from 55 to nearly 74%. The driest air is observed just following ridge passage. The region of moist air tilts eastward with height, being found in advance of the trough at lower levels and to the rear at higher levels. The isopleths are drawn for humidities measured with respect to a plane water surface. Above 300 mb, where the temperature is colder than −30C, the ice phase should predominate. The figures in brackets at the top of the diagram give the time-average relative humidities at 300 mb relative to ice. These suggest that the relative humidity is more uniform in the vertical than the analysis indicates.

d. *Soundings*

The mean temperature profile and the mixing ratio curves for the soundings representing the extremes in moisture are shown in Fig. 7. On the scale shown, it would be difficult to separate by eye the corresponding extreme temperature profiles because of the aforementioned smallness of the temperature deviations.

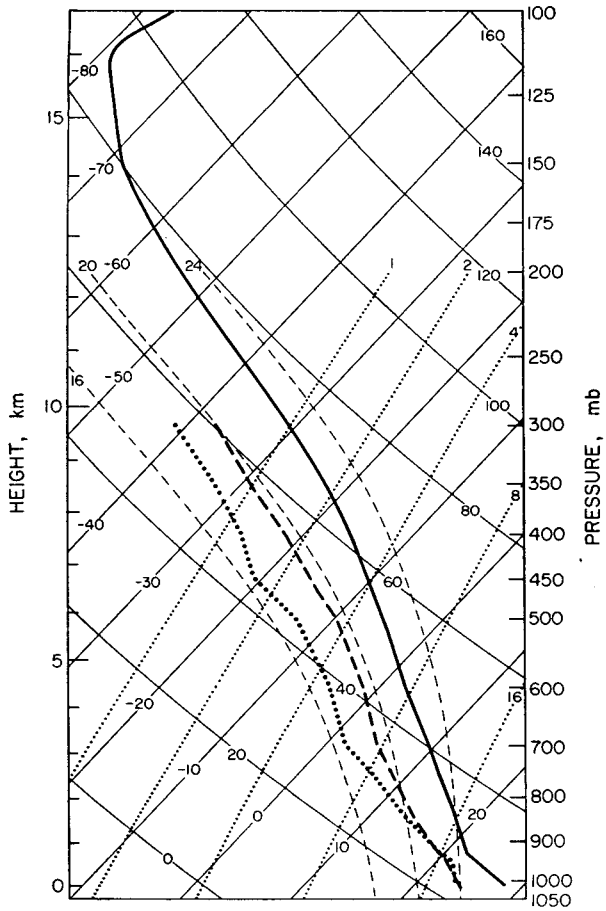

FIG. 7. Average temperature sounding for KEP and moisture soundings for the driest and wettest wave categories, 1 and 5, respectively. Temperature (°C), thin solid lines sloping to right; potential temperature (°C), thin solid lines sloping to left; saturation mixing ratio (gm kg^{-1}) dotted; equivalent potential temperature (°C), dashed.

The temperature curve, which thus may be taken as representative of the mean state in all parts of the disturbance, reveals a sub-cloud layer in which the lapse rate is slightly stable with respect to the dry adiabatic surmounted by a deeper layer of enhanced stability in which the lapse rate is well in excess of the moist adiabatic. The conditional instability which exists in this layer is a well-known feature of the lower and middle tropical atmosphere. In the layer 600–500 mb, the lapse rate is neutral with respect to the moist adiabatic. Between 500 and 150 mb the atmosphere is absolutely stable, but with only weak static stability.

The increased moisture in the trough relative to ridge is again apparent. However, the striking feature of the moisture field is the considerable departure from saturation in the trough region, even allowing for the difference between ice and water saturation. As will be shown later, this is the region of heaviest rainfall. The existence on the synoptic scale of relative humidities well below saturation in the layer below 600 mb could be inferred in advance from the maintenance of the nearly constant conditionally unstable lapse rate in that layer. Only above 600 mb (4 km) is it possible for extensive layer clouds to persist in a stable or neutral environment, but evidently, at least to heights of 300 mb (9 km), such clouds do not exist in sufficient amount to produce saturation over an extensive area. From satellite photographs, it would appear that saturation can be achieved over vast areas at higher levels, presumably near 175 mb (13 km), where the outflow from the tops of cumulonimbus clouds is observed to form large cirrus shields or cloud clusters, as they are now called.

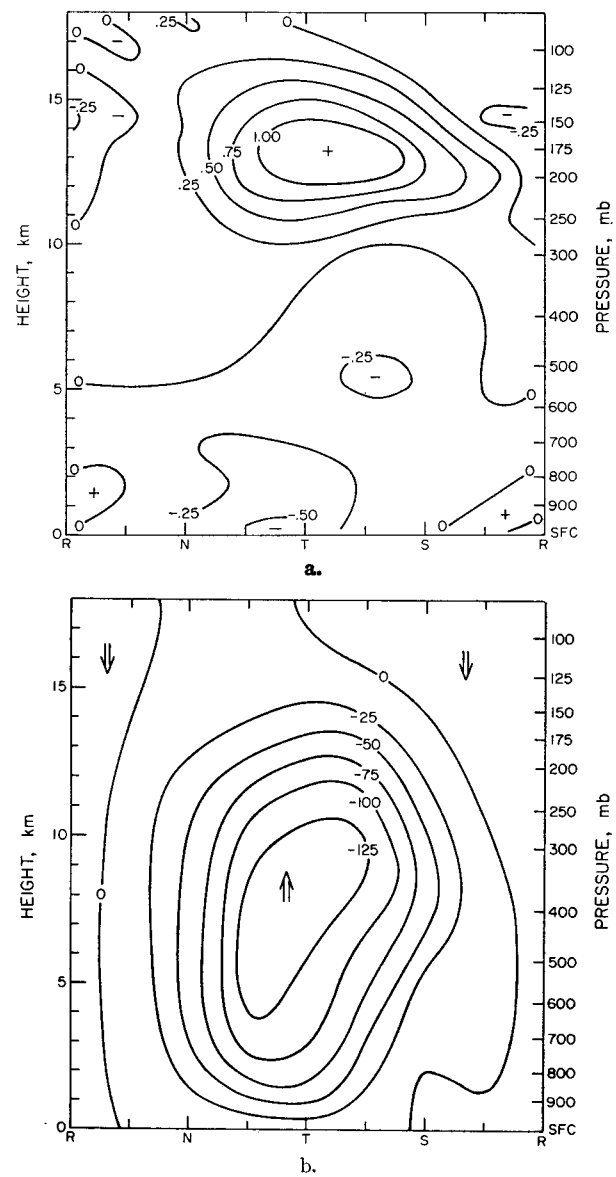

FIG. 8. Composite of horizontal velocity divergence (10^{-5} sec^{-1}) for KEP, a., and corresponding vertical p velocity (10^{-5} mb sec^{-1}), b. (Analyzed values give approximate displacement in millbars per day.) See Fig. 4 for further explanation.

Riehl and Malkus (1958), with their "hot tower" concept, were the first to offer an explanation of how mass and moisture could be transported upward in the equatorial trough zone and precipitation released while maintaining a relatively dry environment. The temperature and moisture patterns found in the rain-bearing disturbances of the equatorial western Pacific provide further support for their concept.

e. Divergence and vertical motion

The divergence field computed from the measured winds, as described in Section 2, is shown in Fig. 8a. The strongest convergence, of the order of -5×10^{-6} sec^{-1}, occurs near the surface in the region just ahead of the mean trough position. The main region of convergence slopes upward to the east, and in the layer from 600–300 mb it lies slightly to the rear of the low-level trough position. Only 10–30% of the convergence takes place in the boundary layer (below 900 mb). As required for mass balance, a region of strong divergence overlies the convergence area. The region is centered near the 175-mb level (13 km) where the maximum value exceeds 10^{-5} sec^{-1}. The altitude of this region and its relatively small pressure-depth suggests that it can be attributed to the integrated effect of the spreading of cumulonimbus anvils. A weak, complex pattern of convergence and divergence is found in the ridge. Generally the motion is divergent below 300 mb and convergent above.

Since islands of sufficient size can produce local wind effects, a question may be raised concerning the representativeness of the divergence measurements, particularly at the lower levels. In this regard we note that two of the observing sites are on small atolls, Kwajalein and Eniwetok, which are unlikely to have a significant disturbing effect on the air flow. The third island, Ponape, is roughly circular with a diameter of about 20 km and a maximum elevation of 779 m; its influence, too, is thus likely to be small, at least above 1 km. The moisture budget measurements to be presented later, which indicate good agreement between rainfall at the three stations and the large-scale moisture convergence, suggest that local effects play at most a secondary role.

The vertical motion field which corresponds to the foregoing divergence pattern appears in Fig. 8b. Upward motion predominates; only in the vicinity of the ridge does subsidence occur in the mean, and even here values are small. Maximum upward velocities in excess of 100 mb day^{-1} are observed in the vicinity of the trough. Largest p velocities occur in the 500–400 mb layer. When the density factor is taken into account, it is found that the largest true velocities occur near 300 mb where the magnitude reaches 2.5 cm sec^{-1}.

f. Vorticity

The field of relative vorticity is shown in Fig. 9. It is apparent that cyclonic vorticity predominates at low levels, anticyclonic vorticity at intermediate levels, and cyclonic vorticity at high levels. The maximum cyclonic vorticity of 8×10^{-6} sec^{-1} is found in the trough region at the top of the boundary layer. A low-level maximum of anticyclonic vorticity with magnitude exceeding 10×10^{-6} sec^{-1} is found in the ridge at 700 mb. A second anticyclonic maximum of about equal strength appears at 175 mb midway between the lower level trough and ridge positions.

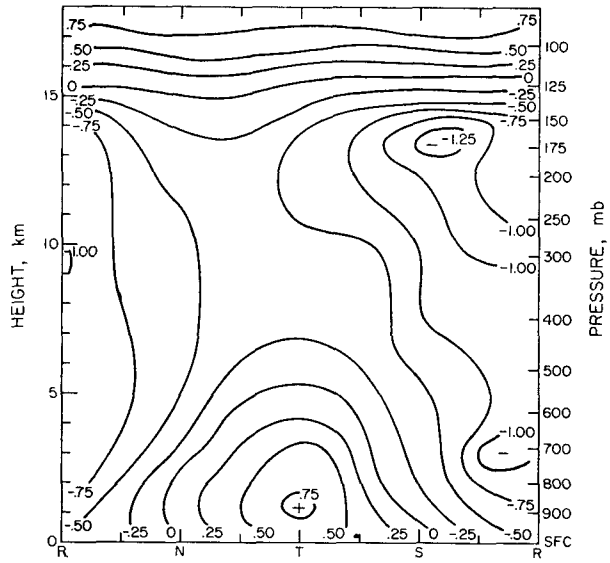

FIG. 9. Composite diagram of vertical component of relative vorticity (10^{-5} sec^{-1}) for KEP. See Fig. 4 for further explanation.

Williams (1970) has inferred from his study of divergence fields in the vicinity of cloud clusters that the meridional (east-west) wind shear contributes much less to the total vorticity than does the zonal (north-south) shear. That this is not true for the low-level vorticity field in the present study can be seen from reference to Fig. 4 which indicates a meridional wind difference of approximately 7 m sec^{-1} in 2000 km (one-half wavelength) or a contribution to the amplitude of vorticity of 3.5×10^{-6} sec^{-1}, as compared with the total amplitude (Fig. 9) of 7×10^{-6} sec^{-1}. Thus, the meridional shear is deduced to be about equal in size to the zonal. Although the difference in results might be due to the different periods studied, it appears more likely that it can be attributed to the difference in methods of compositing, the present study employing the meridional wind field as the basis for averaging in contrast to cloud patterns used by Williams.

In general, however, our results are in good agreement with those of Williams. For example, distributions of vorticities, divergences and vertical p velocities in the trough category of our study are similar to those in his average cloud-cluster category, and the magnitudes of these quantities differ by less than a factor of 2 in all significant respects. It should also be noted that the synoptic-scale divergences and vertical motions mea-

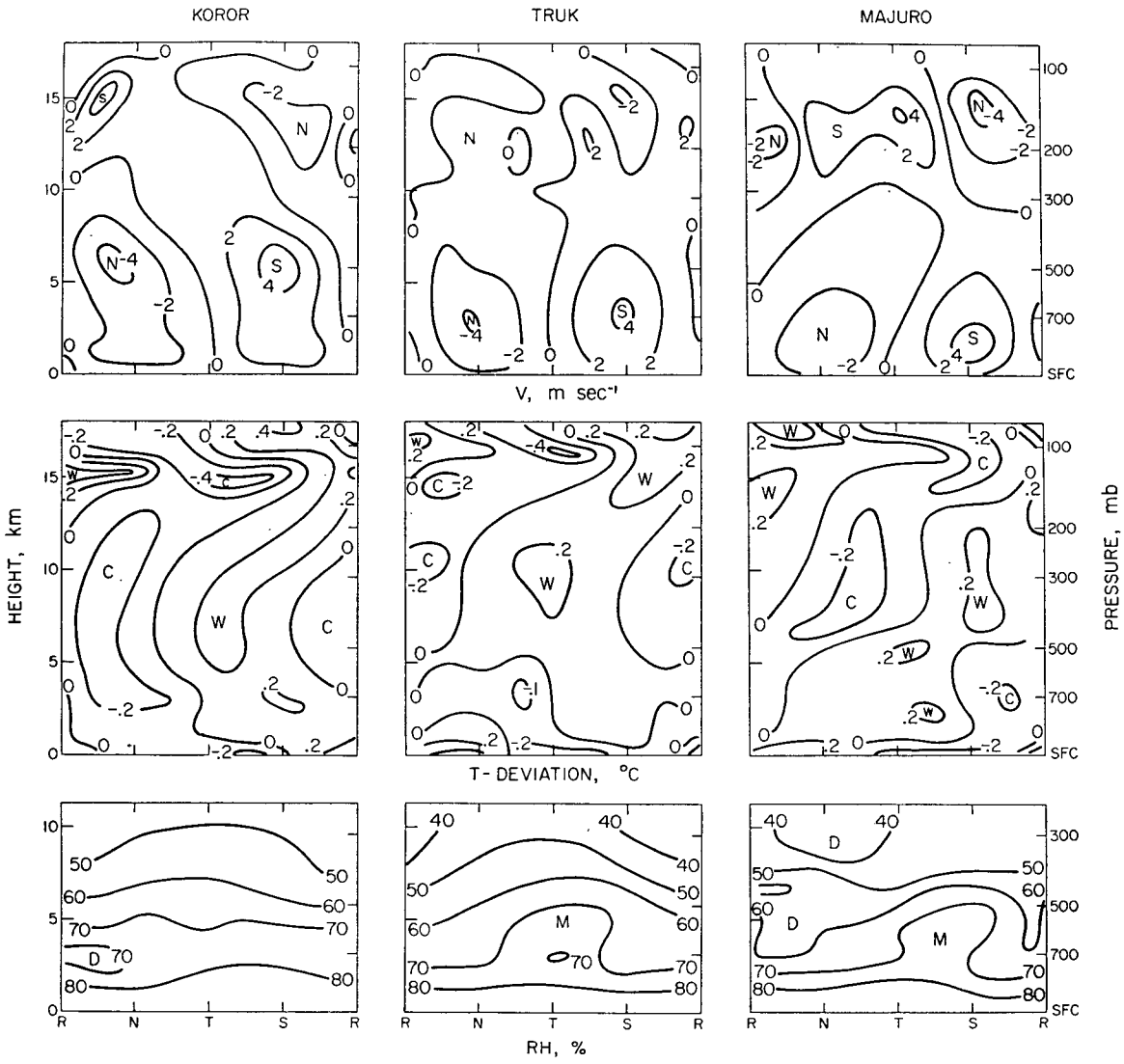

FIG. 10. Composite diagrams of meridional wind component (m sec^{-1}), temperature deviation (°C) and relative humidity for Koror, Truk and Majuro. See Fig. 4 for further explanation.

sured in this study are comparable in size to those obtained from other studies employing direct wind measurement (Yanai and Nitta, 1967; Riehl and Pearce, 1968).

5. Variation of structure with longitude

Both theoretical reasoning and prior observation suggest the possibility of longitudinal variations in wave structure. In this section we examine briefly the observed variations during the three-month period of study. First the meridional wind, temperature and relative humidity fields for Majuro at the eastern end of the region, Truk near the center and Koror at the western end will be compared. Then the relationship of precipitation and cloud amount to the eight wave categories defined previously will be presented for all available stations in the network.

The meridional wind, temperature and relative humidity fields appear in Fig. 10. The fields at Majuro are similar to those already described for KEP. The trough axis leans eastward with height. The upper tropospheric wind fluctuations are somewhat larger than at KEP, and the maxima are displaced slightly to the east. The temperature field shows similar features but is also shifted eastward. The relative humidity field is remarkably like that at KEP.

The wave axis becomes vertical at Truk and the low-level wind maxima and minima appear at a slightly higher level. The upper tropospheric wind structure is chaotic with only the faint suggestion of an opposite variation. The temperature field shows features similar

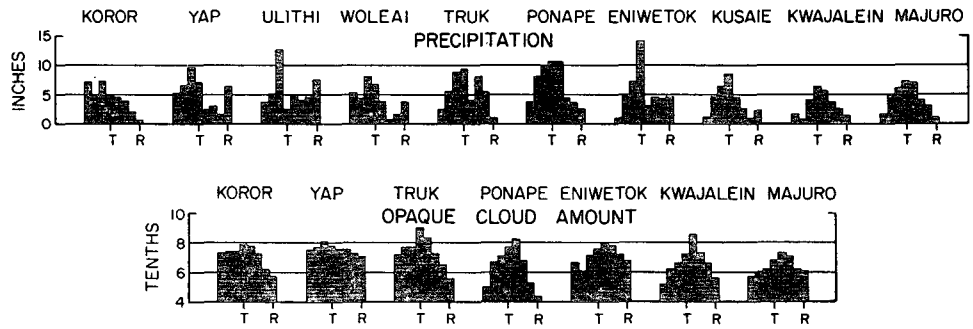

FIG. 11. Total rainfall and average opaque cloud amount as function of wave position for stations in the area of study. T denotes trough axis; R, ridge axis.

to those at Majuro and KEP but displaced a quarter wavelength to the west. The field of relative humidity also is displaced westward with the highest values lying directly over the trough.

The change in tilt of the wave axis continues toward the west so that a reverse, or westward, tilt is observed at Koror. The rise in elevation of the lower wind maximum and minimum also continues with the largest wind fluctuations appearing in the middle troposphere. An opposite wind variation appears again in the upper troposphere. The temperature field resembles closely that at Truk. The relative humidity field, however, shows significant differences. The moist tongue present at Truk and elsewhere at middle levels is nearly absent; the moisture pattern is relatively ill-defined.

The total precipitation in the different wave categories for the three-month period is shown at the top of Fig. 11 and the corresponding opaque cloudiness at the bottom. In general, the position of greatest rain amount shifts from near or slightly east of the trough axis for stations at the eastern end of the network to distinctly west of the axis at the western stations. Most stations exhibit irregularities in the rainfall distribution, suggesting that the period of record is too short to eliminate sampling error. The three- and ten-station averages shown in Fig. 12 are more regular. It is clear that the opaque cloudiness closely parallels the precipitation in its behavior. Cloud amounts are higher overall in the western part of the region.

The variation in position of the rainfall maximum with respect to the wave trough in different parts of the network is similar to that found by Holton (1971) in his diagnostic study of equatorial disturbances, if it is assumed that the point of maximum upward velocity given by the diagnostic model coincides with the rainfall maximum. The variable relationship in Holton's study can be attributed to the different vertical profiles of the zonal wind current which he selected. These were patterned after the observed profiles in the region. It therefore seems reasonable to ascribe the geographical differences in wave structure noted in this section to the large variations in the basic wind current that occur in the region.

A puzzling fetaure that does not seem readily explainable from Holton's results is the nondescript wind pattern in the upper troposphere at Truk. This may be indicative of a transient state which the model cannot reproduce since it gives the wave structure corresponding to a fixed zonal wind profile. We have tacitly assumed in the previous discussion that the wave structure immediately adjusts to variations in zonal current so that the results for the different fixed states apply to successively different states. Another possible explanation is variation in structure with time at Truk itself. The compositing technique, it will be recalled, is based on the lower level wind fluctuations. If, as a result of time variations in zonal wind structure, the upper level fluctuations bear a variable relationship to the lower, they will be much reduced in the composite picture. This effect should be particularly pronounced at Truk since it lies in the zone where the zonal current undergoes its most rapid variation.

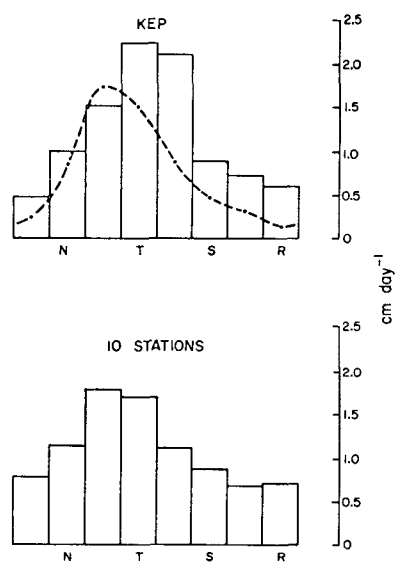

FIG. 12. Observed average rainfall (cm day^{-1}) in various sectors of wave for KEP (top), with rainfall computed from moisture budget being given by the dashed line. Observed average rainfall for all stations in the network is shown in the lower part of the figure.

TABLE 1. Computed moisture budget (cm day^{-1}). Category 4 is centered on the trough axis, category 8 on the ridge.

	Category								
	1	2	3	4	5	6	7	8	Mean
Storage	−0.25	−0.36	−0.06	−0.02	0.01	0.28	0.30	0.11	0
Advection	0.09	0.18	−0.04	−0.18	−0.35	−0.30	−0.30	−0.14	−0.13
Convergence	0.17	0.76	1.52	1.38	0.83	0.17	0.07	−0.10	0.60
Sum $=P-E$	0.01	0.58	1.42	1.18	0.49	0.15	0.07	−0.13	0.47
Evaporation	0.25	0.27	0.32	0.35	0.39	0.32	0.26	0.26	0.30
Precipitation	0.26	0.85	1.74	1.53	0.88	0.47	0.33	0.13	0.77

In concluding this discussion of the wave structure, we note that our description is consistent in all respects with the results obtained recently by Wallace (1971) from application of spectral techniques to the overlapping period July–October 1967.

6. Moisture budget

In this section we compare the observed precipitation at Kwajalein, Eniwetok and Ponape during the different phases of the wave with the precipitation within the enclosed area computed from the principle of the continuity of water substance. Since the computed precipitation depends mainly on the horizontal velocity convergence into the area, the comparison provides a good test of the reliability of the previous estimates of divergence, vertical velocity and vorticity.

If q is the specific humidity, the continuity of water substance requires that

$$C=-\frac{dq}{dt}=-\left(\frac{\partial q}{\partial t}+\nabla\cdot q\mathbf{V}+\frac{\partial}{\partial p}q\omega\right), \qquad (1)$$

where C is the net rate of condensation in grams of water per gram of air per unit time t, $\mathbf{V}$ the horizontal wind, p the vertical coordinate, and ω the vertical pressure-velocity. Averaging the terms in (1) for all observations in a wave category and integrating with respect to pressure from the ocean surface, where the vertical moisture flux is denoted by E (the surface evaporation) to a height in the upper troposphere where the vertical flux is negligible (assumed here to be 300 mb), we obtain

$$P-E=\underbrace{g^{-1}\frac{\partial}{\partial t}\int_{p_0}^{300}\bar{q}dp}_{S}+\underbrace{g^{-1}\int_{p_0}^{300}\overline{\mathbf{V}\cdot\nabla q}dp}_{A}+\underbrace{g^{-1}\int_{p_0}^{300}\overline{q\nabla\cdot\mathbf{V}}dp}_{D}, \qquad (2)$$

where g is the acceleration of gravity and the bar denotes the category average.

This equation states that $P-E$, the average difference between the precipitation and evaporation in a particular category, equals the sum of the moisture storage S, the moisture advection A, and the moisture divergence (convergence) D. The quantities S, A and D apply to water vapor only; moisture in condensed form has been neglected in the present formulation. The expansion of the moisture divergence term in (1) into moisture advection and velocity divergence terms in (2) was done in order to assure that total mass continuity was not violated. The trapezoidal rule was applied to data from 13 pressure levels from the surface to 300 mb, inclusive, in performing the vertical integration. The average moisture storage in each of the eight wave categories was computed from the difference in the precipitable water contents of the immediately preceding and following categories. The change, or storage, is expressed in centimeters day^{-1}, with the assumption of an average time difference between every second category of $1\frac{1}{4}$ day. Only nighttime humidities were used in evaluating the precipitable water content.

The average moisture advection in each category is based on individual advection measurements obtained from the twice-daily radiosonde reports, except that linearly interpolated humidities were used in the daytime. The advection was calculated from a computer program which determined the wind vector and specific humidity gradient at the center of the triangle from wind velocities and specific humidities at the corners, with the assumption of linear variations of the wind and humidity fields within the region. The average value of the convergence term for each category was evaluated from the appropriate 12-hr values of specific humidity and velocity divergence, again with use of interpolated humidities for daytime observations.

The results of the calculations are shown in Table 1 and are compared with measured precipitation in Fig. 12. Since the sum of the three terms yields the difference between the precipitation and evaporation, it has been necessary to estimate the evaporation in order to make the comparison. The familiar formula for evaporation from a water surface under conditions of neutral stability was employed. This has the form

$$E=\rho C_D(q_0-q_a)V, \qquad (3)$$

where ρ is the air density, C_D the drag coefficient, q_0 the saturation specific humidity appropriate to the ocean surface temperature, q_a the actual specific

humidity at instrument level, and V the wind speed. The average evaporation in each category was determined from the appropriate twice-daily measurements of wind speed and humidity with ρ and q_0 assumed to have the constant values 1.15×10^{-3} gm cm^{-3} and 24.4 gm kg^{-1} (surface temperature 28.5C), respectively, and from the following assumed variation of C_D with wind speed (Roll, 1965):

$$C_D=(1.10+0.04V)\times10^{-3}, \qquad (4)$$

where V is in meters per second.

From Table 1 it is seen that the storage and advection terms are generally small, being less than 5 mm day^{-1} in all categories. Their sum is still smaller, in no case exceeding 2 mm day^{-1}. Ahead of the trough the sum is positive, signifying that more moisture is advected into this portion of the wave than is stored. The opposite effect occurs just to the rear of the trough axis where more moisture is lost by advection than is removed from the column. In the categories near and ahead of the trough axis the convergence term is by far the largest. The sum of the three terms exhibits a large variation with position in the wave and is even slightly negative in the south wind category, though by such a small margin as to be doubtful in sign. The evaporation is estimated to average 0.3 cm day^{-1}, and to vary by nearly 50% with largest values occurring in the vicinity of the trough. Inspection of daily values reveals that the variation with category is due almost entirely to the greater frequency of above average wind speeds in the troughs than in the ridges.

Addition of the evaporation to the previous sum yields the estimated precipitation shown in the bottom row. The computed amounts may be compared with the observed by reference to Fig. 12 where the average observed daily precipitation by category for the three principal stations is shown at the top and the average for all 10 stations in the area of study is shown at the bottom. As can be seen from Fig. 11, which depicts the precipitation regime for individual stations, the three-month sample is too small, in general, to yield a smooth relationship with the wave. Thus, it seems possible that the average precipitation for the three stations used in the moisture budget computation may not necessarily give a better estimate of the average precipitation in the triangle than an average based on a greater number of stations even though some are quite distant from the region in question. Both the three- and ten-station averages are based on the wave chronology of the individual stations involved, not on the chronology for the center of the triangle.

If account is taken of the uncertainty in the observed precipitation, it can be said that computed and observed amounts are in good agreement. The only significant difference appears to be a deficiency in computed amounts in most categories. No reason for this difference is apparent unless evaporation values are too small. However, its seems unlikely that the estimated evaporation can be wrong by a factor of 2 as required to explain the difference on this basis. Even the occurrence of superadiabatic lapse rates between observation hours with an associated increase in moisture flux would not have a sufficient effect in this respect (Hoeber, 1970).

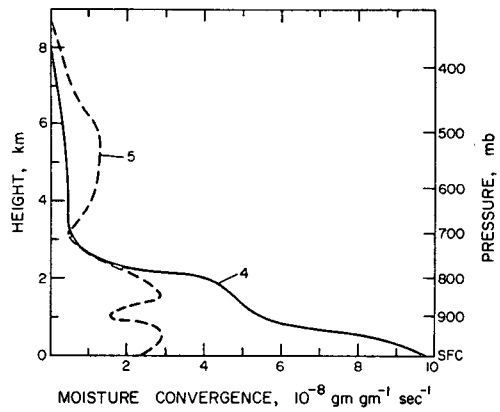

FIG. 13. Moisture convergence (10^{-8} gm gm^{-1} sec^{-1}) as a function of height in wave categories 4 and 5. (See text for discussion.)

Of importance in connection with the problem of incorporating latent heat release by deep convection in numerical prediction models for the tropics is the question of what fraction of the synoptic-scale moisture convergence occurs in the planetary boundary layer. It is thus of interest to examine the vertical distribution of moisture convergence [term D in Eq. (2), the product of the specific humidity and divergence] in the wave disturbance. This is shown in Fig. 13 for categories 4 and 5, two of the categories in which substantial amounts of rain fell. Clearly only a fraction of the total convergence occurs in the boundary layer, if this layer is assumed to extend to the typical height of 1 km. In category 4, 60% of the convergence occurs below this height; in category 5, only 30%. These results are consistent with the findings of Williams (1970).

However, it should not be concluded from these results and those previously reported on mass convergence that the boundary layer supplies only a small fraction of the mass and moisture that is carried aloft in the deep convection. Indeed, only air from the boundary layer has sufficient buoyancy to reach the upper-level divergent region, centered at 175 mb, which marks the region of cirrus outflow. From the equivalent potential temperature distribution, it can be inferred that at most one gram of environmental air is entrained per two grams of cloud air in ascending from the boundary layer to the outflow region. The answer to the dilemma lies in the fact that downdrafts and ambient subsidence also transport mass and moisture into the boundary layer, that is, a portion of the mass and moisture which converges aloft enters the boundary layer rather than the rising cloud mass.

TABLE 2. Heat budget (°C day^{-1}) for different parts of the wave based on a simple model. The terms S, A and B represent contributions to diabatic heating H by storage, horizontal advection and vertical motion, respectively; R is the net radiative change.

Level	North				Trough				South				Ridge				
(mb)	S	A	B	H	S	A	B	H	S	A	B	H	S	A	B	H	R
900	0	−0.1	0.8	0.7	−0.2	0.1	2.0	1.9	0	−0.1	−0.1	−0.2	0.2	0.1	−0.2	0.1	−1.0
800	0	−0.4	1.3	0.9	−0.2	0	3.5	3.3	0	−0.1	0	−0.1	0.2	0	−0.7	−0.5	−1.1
700	−0.4	−0.1	2.3	1.8	−0.1	0	4.4	4.3	−0.1	0	0	−0.1	0.5	−0.3	−0.5	−0.3	−1.2
600	−0.1	0.2	3.5	3.6	−0.1	0	5.4	5.3	−0.1	−0.1	0.6	0.4	0.2	−0.1	−0.2	−0.1	−1.2
500	0.3	0	3.9	4.2	−0.2	−0.1	6.6	6.3	−0.1	0.2	1.8	1.9	0.2	0	−0.3	−0.1	−1.3
400	0.2	0.1	3.1	3.4	0.1	−0.1	6.4	6.4	−0.2	0.2	2.3	2.3	0	−0.1	−0.7	−0.8	−1.4
300	0.2	0	2.0	2.2	0.2	−0.1	4.6	4.7	−0.2	0	2.0	1.8	−0.2	0.1	−0.7	−0.8	−1.5
200	0	0.7	0.8	1.5	0.1	−0.4	2.1	1.8	0	−0.3	0.6	0.3	−0.1	0.7	−0.2	0.4	−0.5
150	−0.3	2.2	1.3	3.2	−0.2	0	2.3	2.1	0.4	1.3	−0.5	1.2	0.1	0.7	−0.3	0.5	0
100	0.2	1.2	2.1	3.5	−0.2	0.6	0	0.4	−0.2	0	−2.8	−3.0	0.2	0.4	0	0.6	0.3

Cumulus convection thus carries considerably more mass and moisture upward than is indicated by the synoptic-scale horizontal convergence into the boundary layer. Similar arguments were advanced earlier by Riehl and Malkus (1958).

7. Heat budget

It is now generally agreed that latent heat release provides the major source of energy for many tropical disturbances, and it has been recently speculated (Frank, 1970) that radiative differences may also provide a significant thermal drive for some types of disturbances. The pattern of diabatic heating in the tropical wave disturbances of the equatorial western Pacific is thus a matter of considerable interest. We will now attempt to deduce the heating distribution. In so doing, we will consider first a simple model in which synoptic-scale parameters alone are used to estimate the heating. Then we will attempt to arrive at a more realistic pattern by setting up a model in which regions of convective updrafts and downdrafts and the intercloud or ambient region are treated separately.

The diabatic heating rate, expressed in units of the rate of temperature change, may be written from the thermodynamic energy equation as

$$\underbrace{\frac{1}{c_p}\frac{dh}{dt}}_{H}=\underbrace{\frac{\partial T}{\partial t}}_{S}+\underbrace{\mathbf{V}\cdot\nabla T}_{A}+\underbrace{\omega\left(\frac{\partial T}{\partial p}-\frac{\alpha}{c_p}\right)}_{B}, \tag{5}$$

where c_p is the specific heat at constant pressure, h the heat added per unit mass, T temperature, α specific volume, and the other variables are defined as before. The diabatic heating H is thus the sum of three terms: a storage term S, a horizontal advection term A (negative of the advection as ordinarily defined), and a vertical motion term B which expresses the difference between the vertical temperature advection and the dry adiabatic cooling.

The average diabatic heating obtained by summing the average values of these three terms is given in Table 2 for several categories. The storage and advection terms were derived in the manner described for the corresponding terms in the moisture budget. The vertical motion term at any level was computed from the product of the average synoptic-scale vertical p velocity and the average value of the static stability parameter, $(\partial T/\partial p-\alpha/c_p)$, as determined from the mean sounding shown in Fig. 7. This procedure is not fully justified since on the synoptic scale term B must be regarded as a spatial average of the product of the vertical motion and the stability parameter and not as the product of the spatial averages of these quantities. But inasmuch as the lapse rate within the convection does not differ greatly from that in the ambient air, the error introduced by this assumption is small, and our results should give a good first approximation to the heating profiles. The model to be considered subsequently is designed to overcome the shortcoming of this assumption.

From the table it is evident that the vertical motion term is by far the most important in determining the heating pattern. The strongest heating, of the order of 6C day^{-1}, occurs in the layer 500–400 mb slightly in advance of the trough (category 4). Cooling is very weak and confined almost entirely to the ridge area. The computations were not extended below 900 mb because of the difficulty of estimating the flux of sensible heat by small-scale turbulence in the sub-cloud layer where it could conceivably be an important process (Garstang, 1967).

The final column in the table gives net radiative cooling rates R obtained from smoothed profiles of infrared cooling rates and shortwave heating rates for the equator in July appearing in Dopplick (1970). The heating due to latent heat release may be obtained by subtracting these values from the figures for total diabatic heating. It is probable that the net radiative cooling differs somewhat between trough and ridge, but the effect is not likely to be large and will be neglected here.

The foregoing computations, and the earlier moisture budget computations, are based on the assumption that the measurements yield essentially synoptic-scale

values of the variables and that the terms in (2) and (5) can be evaluated from these values alone. It is well known, however, that when more than one scale of motion is present, terms involving products of the variables, i.e., nonlinear terms, cannot be evaluated from the products of the large-scale variables alone unless the smaller scale fluctuating quantities are uncorrelated. Following Charney and Eliassen (1964), we will assume that the small- or convective-scale temperature and moisture fluctuations are correlated only with the vertical component of the velocity fluctuations. With this assumption only term B of (5) requires further consideration and re-evaluation.

To recompute this term and thereby determine the effect of convection on the heating profile, we will make use of a highly idealized model based on the hot tower concept of Riehl and Malkus. In the model we assume that the convective updrafts are undilute and that the updrafts and downdrafts occupy only a small volume, of the order of 1–10%, within a larger ambient volume which is essentially cloud free and gently subsiding. The latter assumption is believed to be reasonable even in the distributed part of the wave. It is supported by a variety of evidence including radar measurements in a well-developed easterly wave in the Caribbean which indicated that only 2% of the disturbed area was occupied by hard echoes and 10% by soft echoes (Krishnamurti, 1968). A schematic diagram of the model, with updraft and downdraft areas greatly exaggerated relative to the ambient region, is depicted in Fig. 15a.

We next note that the synoptic-scale vertical p velocity, regarded as an average value over an area A of suitable size, may be written as

$$[\omega]=\frac{A_u[\omega_u]+A_d[\omega_d]+A_a[\omega_a]}{A}, \tag{6}$$

where $[\omega_u]$, $[\omega_d]$ and $[\omega_a]$ represent the space average or typical vertical motions in the updraft, A_u, downdraft, A_d, and ambient, A_a, regions. Alternatively, for simplicity and as a conceptual aid, (6) may be written as

$$\omega=\omega_u+\omega_d+\omega_a, \tag{7}$$

where ω_u, ω_d and ω_a denote the average vertical motions *with respect to the total area* in the updraft, downdraft and ambient regions, respectively. In other words, ω_u is the typical vertical motion in the updrafts multiplied by the ratio of the area occupied by updrafts to the total area, etc. Since $\omega\approx -g\rho w$, where w is the vertical velocity, the ω's on the right-hand side of (7) more properly may be regarded as representing the contributions of the separate regions to the net vertical mass flux. Using this concept, the contribution to the average or synoptic-scale diabatic heating by term B in (5) is seen to be

$$B=\frac{A_u[\omega_u]\sigma_u+A_d[\omega_d]\sigma_d+A_a[\omega_a]\sigma_a}{A}$$

$$=\omega_u\sigma_u+\omega_d\sigma_d+\omega_a\sigma_a, \tag{8}$$

where

$$\sigma_{u,d,a}\equiv\left(\frac{\partial T}{\partial p}-\frac{\alpha}{c_p}\right)_{u,d,a}$$

denotes the static stability parameter, the subscripts indicating that a single typical value is to be applied in each region.

The following steps were followed in evaluating the quantities in (8) and redetermining the overall diabatic heating, H:

1) In the assumed absence of condensation and internal evaporation in the ambient region, the radiative cooling must be balanced by the sum of the storage, advection and vertical motion term, $\omega_a\sigma_a$. Thus, if the fractional area of the ambient region is approximated by unity, Eq. (5) may be applied to synoptic-scale parameters to obtain ω_a. It seems reasonable to suppose that the observed synoptic-scale values closely approximate ambient values because of the small probability that the radiosondes sampled regions of convective activity.

2) The moisture budget for the ambient region is next computed from the synoptic-scale wind and moisture measurements and the values of ω_a obtained in step (1). Thus,

$$\left(\frac{dq}{dt}\right)_a=\frac{\partial q}{\partial t}+\mathbf{V}\cdot\nabla q+\omega_a\left(\frac{\partial q}{\partial p}\right)_a, \tag{9}$$

where the term on the left represents the rate of moisture addition required to maintain balance. This term is found to be positive everywhere indicating that a source of moisture is needed to keep the ambient region from drying out. Ultimately, the moisture must be supplied by evaporation of cloud droplets and precipitation.

3) To make the problem tractable, we assume that the moisture loss in the ambient region is replenished through exchange with air that has been moistened by evaporation in unsaturated downdrafts, that is, we imagine a statistically steady state in which masses of ambient air are successively incorporated in downdrafts, moistened, and then re-incorporated in the intercloud region. The average downdraft speed ω_d can be determined from the inferred evaporation by assuming that the temperature of the downdraft is just sufficient to maintain negative buoyancy, that is, its temperature is equal to the ambient temperature. Although this assumption is made mainly for convenience, it is believed to be approximately true for the conditions which exist in tropical convection (Kumburova and

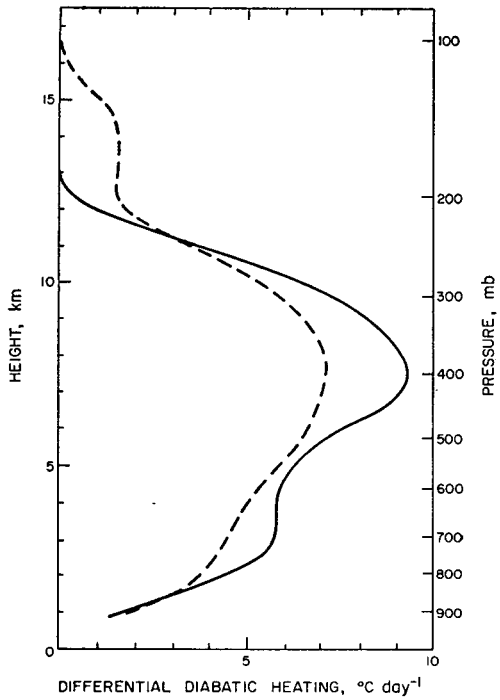

FIG. 14. Diabatic heating difference between trough and ridge areas: solid line, model with effects of convection included explicitly; dashed line, simple model.

Ludlam, 1966). Conserving wet bulb potential temperature under this assumption, one can easily determine from an adiabatic chart the area-average subsidence required to add a specified amount of moisture by evaporation.

4) Eq. (7) may now be solved for ω_u, the average updraft velocity. The product $\omega_u\sigma_u$ then gives the heating by condensation. The value of the static stability parameter at the various levels was taken from the moist adiabat which passes through the temperature (22C) and pressure (940 mb) of the top of the sub-cloud layer (equivalent potential temperature of 355K). A saturated undilute parcel rising moist adiabatically from this point becomes negatively buoyant at about 150 mb, close to the level of maximum cirrus outflow as deduced from the measured divergence pattern. Starting from a slightly different point or allowing for sufficient entrainment to terminate the positive buoyancy at 200–175 mb has little effect on the results.

5) Addition of the latent heat release, the evaporative cooling and the radiative cooling then yields the total diabatic heating.

In summary, our procedure has been to evaluate first ω_a and $\omega_a\sigma_a \equiv B_a$ by applying (5) to the ambient region where $H=R$, the radiative heating rate. Thus,

$$\omega_a\sigma_a = R - S - A. \tag{10}$$

From the moisture budget in the ambient region and the assumptions stated in step 3), ω_d and $\omega_d\sigma_d \equiv I$ (the heating rate due to internal evaporation) were determined. It was then possible to calculate ω_u from (7) and obtain $\omega_u\sigma_u \equiv L$ (the heating rate due to condensation). Finally, (5) was used to determine the total diabatic heating H. Thus,

$$\begin{aligned} H &= S + A + B = S + A + \omega_u\sigma_u + \omega_d\sigma_d + \omega_a\sigma_a \\ &= S + A + L + I + (R - S - A) = L + I + R. \end{aligned} \tag{11}$$

An abbreviated summary of the calculations for the trough and ridge categories is given in Table 3, and the difference in diabatic heating between trough and ridge, which constitutes the thermal drive, is depicted in Fig. 14. Also shown is the curve derived earlier on the basis of the simpler model.

According to the present formulation, the main effect of taking explicit account of the convection in computing the diabatic heating is to increase the magnitude of the heating maximum near 400 mb by about 2C day^{-1} and to diminish the rate above 250 mb by a somewhat smaller value. The enhanced heating at

TABLE 3. Heat budget (°C day^{-1}) for model with convection. New terms are B_a, the adiabatic heating by ambient vertical motion; L, condensation heating; I, internal evaporative heating; and H, total diabatic heating. Other components of the heat budget are as given in Table 2. Also shown are area-mean vertical p velocities (ω's) in cgs units for ambient a, downdraft d, and updraft u regions, and the overall average or synoptic value.

Level	Trough								Ridge							
(mb)	ω_a	ω_d	ω_u	ω	B_a	L	I	H	ω_a	ω_d	ω_u	ω	B_a	L	I	H
900	0.23	0.46	−1.20	−0.51	0.9	5.7	−2.4	2.3	0.32	0.81	−1.08	0.05	1.3	5.1	−3.4	0.7
800	0.22	0.29	−1.36	−0.85	0.9	6.8	−1.4	4.3	0.32	0.57	−0.73	0.16	1.3	3.7	−2.6	0
700	0.25	0.35	−1.62	−1.02	1.1	9.2	−1.9	6.1	0.32	0.35	−0.55	0.12	1.4	3.1	−1.7	0.2
600	0.22	0.46	−1.67	−1.09	1.1	9.8	−2.4	6.2	0.26	0.23	−0.45	0.04	1.3	2.6	−1.2	0.2
500	0.18	0.35	−1.72	−1.19	1.0	10.6	−1.7	7.6	0.27	0.23	−0.45	0.05	1.5	2.8	−1.2	0.3
400	0.27	0.35	−1.88	−1.26	1.4	11.1	−1.4	8.3	0.25	0.17	−0.28	0.14	1.3	1.6	−0.7	−0.5
350	0.39	0.35	−2.02	−1.28	1.8	10.8	−1.4	7.9	0.35	0.23	−0.41	0.17	1.6	2.2	−1.0	−0.3
300	0.41	0.23	−1.91	−1.27	1.6	8.4	−0.7	6.2	0.36	0.17	−0.34	0.19	1.4	1.5	−0.7	−0.7
250	0.48	(0.12)*	−1.73	−1.13	1.6	6.4	(−0.5)*	4.5	0.47	(0.12)*	−0.43	0.16	1.6	1.6	(−0.2)*	0
200	0.10	—	−0.87	−0.77	0.2	0.5	—	0	0.53	—	−0.42	0.11	1.1	0.3	—	−0.2
150	−0.02	—	−0.25	−0.27	−0.2	—	—	0	0.09	—	−0.05	0.04	0.8	—	—	0
100	0	—	0	0	0.1	—	—	0.3	0	—	0	0	0.3	—	—	0.3

* Values in parentheses were obtained by extrapolation of dew point curves.

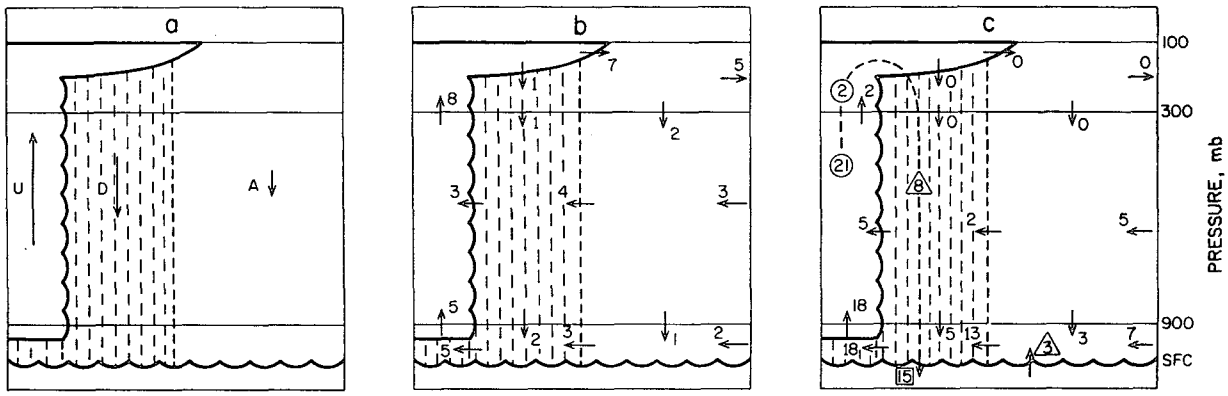

FIG. 15a. Model used in calculating heat budget with convection, where U is the updraft region, D the downdraft and A ambient. Areas of U and D are greatly exaggerated with respect to A. b. Schematic mass budget in arbitrary relative units. c. Schematic moisture budget in arbitrary relative units, where circles indicate condensation, triangles, evaporation, and the square the precipitation reaching the surface.

middle levels can be attributed to the fact that the area-average upward motion in convection is considerably greater than the net upward motion used in the previous calculation (compare columns 4 and 5 of Table 3), while the static stability in the convective updrafts does not differ much from the ambient static stability used previously. Thus, the computed latent heat release is larger when convection is considered. On the other hand, the computed latent heat release above 250 mb is smaller when convection is treated explicitly, since the moist adiabatic lapse rate differs less from the dry adiabatic than does the ambient lapse rate. The latter was employed in the previous formulation which ignores convection, and its use results in an overestimate of the adiabatic cooling and hence of the compensating latent heat release.

In view of the admitted shortcomings of the assumptions employed, the diabatic heating profile in Fig. 14 must be regarded as tentative. Even so, for the reasons given above, its shape is almost certainly more realistic than that determined from large-scale parameters alone. The columns marked L and I in Table 3 give internal condensation and internal evaporative heating, respectively. The precipitation, which can be calculated from their difference, is in good agreement with the observed precipitation for these categories. Comparison of L and I indicates that $\sim$75% of the condensed moisture falls to the ground as precipitation in the trough region and only 40% in the ridge. These appear to be reasonable values for convection in typically disturbed and undisturbed conditions. The area-average updraft velocities in the disturbed region range from about 1 cm sec^{-1} near the cloud base to 5 cm sec^{-1} at 300 mb. If 2% of the area is occupied by active convection, these correspond to updraft velocities in individual cumulus of 2–10 m sec^{-1}.

We conclude this section by showing schematic mass and moisture budgets in Figs. 15b and c for the trough category derived on the basis of the foregoing model. The diagrams are presented for the purpose of summarizing the results of the calculations and for illustrating basic aspects of the problem. Because of model limitations, such as the neglect of entrainment and the assumption that all re-evaporation takes place in unsaturated downdrafts, we do not intend them to represent an exact description of the convective-synoptic scale interaction process. The mass budget is based on the ω's given in Table 3. The moisture budget was obtained from the ω's and values of specific humidity, precipitation and surface evaporation presented earlier. The diagrams depict graphically the manner in which more mass and moisture can be transported upward from the boundary layer than are provided by synoptic-scale horizontal convergence into the layer. Though explicit account was not taken of entrainment in the model calculations, it will be noted that mass balance requires an entrainment of roughly one unit of ambient air per two units of air entering the updraft from below.

8. Summary and conclusions

The main findings of the present study are as follows:

1) During the three-month period July–September 1967, 18 weak synoptic-scale disturbances with average wavelengths of 3500–4000 km traveled westward at an average speed of 7° longitude day^{-1} (9 m sec^{-1}) in the equatorial trough zone of the western Pacific. The disturbances were readily recognizable on time-longitude strip charts constructed from digitized satellite mosaics.

2) In the region near 160E, where the mean zonal wind varied nearly monotonically from 1 m sec^{-1} easterly at the surface to 9 m sec^{-1} easterly at 100 mb, the waves exhibited the following features:

(i) Meridional wind fluctuations were strongest near 800 mb (3–4 m sec^{-1} amplitude) and 175 mb (2–3

m sec^{-1}). The upper and lower fluctuations were nearly out of phase.

(ii) Temperature fluctuations were 1C or less at all levels. Pronounced cool anomalies occurred at lower levels in the region just behind (to the east of) the trough and in the upper troposphere above the trough. A region of warm anomaly, centered at 300 mb, was observed between.

(iii) Relative humidities were highest in the vicinity of the trough and lowest in the ridge. Values ranged from about 55–75% in the middle troposphere, indicating an absence of large-scale saturation even in the most disturbed part of the waves.

(iv) The maintenance on the synoptic scale of conditionally unstable lapse rates and non-saturation in disturbed regions supports the hypothesis that condensation takes place in undilute cumulus towers, as proposed by Riehl and Malkus (1958).

(v) Convergence predominates at low levels in the waves. The largest value, -5×10^{-6} sec^{-1}, occurs at the surface near the wave axis. The level of non-divergence varies from 500 to 300 mb. A region of strong divergence with maximum value of 11×10^{-6} sec^{-1} is centered at 175 mb above the low-level trough position. This is believed to be close to the level of cirrus outflow from cumulonimbus towers, suggesting that the synoptic-scale divergence represents the collective outflow from cumulonimbus clusters.

(vi) The vertical motion is upward everywhere except in the vicinity of the low level ridge. Maximum vertical p velocity of about 120 mb day^{-1} (5 mb hr^{-1}) occurs near 400 mb in the region of the trough axis. The maximum vertical velocity of 2.5 cm sec^{-1} occurs at 300 mb in about the same position.

(vii) The vorticity has its maximum variation in the lower troposphere (900–700 mb) with values ranging from 8×10^{-6} sec^{-1} in the trough to -12×10^{-6} sec^{-1} in the ridge. A second region of large variation is found near 175 mb where the vorticity ranges from -3×10^{-6} sec^{-1} in the region above the surface northerly wind components to -13×10^{-6} sec^{-1} above the surface southerlies.

3) The structure of the waves undergoes a systematic change as they travel from the easternmost to the westernmost islands. The wave axis, which tilts eastward with height at the eastern end of the network, becomes vertical in the central region and acquires an opposite tilt in the west. Temperature and humidity fields are displaced progressively westward relative to the wind field. Precipitation and opaque cloudiness variations also change in a systematic fashion across the network. Cloud amounts are generally higher to the west, and precipitation and cloud maxima tend to occur to the east of the trough axis at eastern stations and to the west of the axis at western stations. The change of wave structure is believed to be caused by the variation with longitude of the vertical shear of the basic current (Holton, 1971).

4) Precipitation estimated from the moisture budget is in good agreement with observed precipitation. In the disturbed region of the wave, where precipitation is heaviest, the mass convergence term is the principal contributor to the budget.

5) The diabatic heating profiles estimated by methods which do and do not take explicit account of the convection give rather similar results. The difference in heating between trough and ridge regions attains a maximum value of about 8C day^{-1} at 400 mb. The heating differential is small above 200 mb.

The findings enumerated above have obvious implications in the development of numerical models of the tropical atmosphere and raise questions regarding both the convective adjustment hypothesis and the CISK hypothesis on which current models are based (Manabe *et al.*, 1970; Ooyama, 1969). We find that the large-scale tropical atmosphere does not become absolutely unstable and readjust, as in the convective adjustment hypothesis. Instead, the vertical heat transport takes place in convective updrafts and downdrafts operating within a conditionally unstable atmosphere (below 500 mb). This point has already been made by Krishnamurti (1969) and others. We also find, in agreement with Williams (1970), that only a fraction of the mass and moisture convergence, *as measured by the synoptic-scale fields*, occurs in the boundary layer (below 900 mb). Moreover, the fraction of boundary layer convergence to total convergence varies with position in the wave, making it difficult to relate the *synoptic-scale* vertical motion at the top of the boundary layer to the latent heat release as most CISK models attempt to do. We do not interpret this result to mean that the convection does not emanate from the boundary layer. Rather it indicates that this layer is occupied by both convergent (updraft) and divergent (downdraft) regions with the synoptic-scale convergence representing only a net value which is not perfectly correlated with the convective scale convergence.

Acknowledgments. Special thanks are due Prof. J. M. Wallace for valuable discussions covering all phases of the work and for reading the manuscript. We would also like to thank Profs. J. A. Businger and J. R. Holton for their interest and advice. The research was supported by the National Science Foundation under Grant GA629X.

REFERENCES

Chang, C.-P., 1970: Westward propagating cloud patterns in the tropical Pacific as seen from time-composite satellite photographs. *J. Atmos. Sci.*, **27**, 133–138.

——, V. F. Morris and J. M. Wallace, 1970: A statistical study of easterly waves in the Western Pacific: July–December 1964. *J. Atmos. Sci.*, **27**, 195–201.

Charney, J. G., and A. Eliassen, 1964: On the growth of the hurricane depression. *J. Atmos. Sci.*, **21**, 68–75.

Colton, D. E., 1970: Comments on "Temperature-induced errors in the ML-476 humidity data." *J. Appl. Meteor.*, **9**, 834–835.

Dopplick, T. G., 1970: Global radiative heating of the earth's atmosphere. Ref. No. 24, Planetary Circulations Project, Dept. of Meteorology, Massachusetts Institute of Technology, 128 pp.

Frank, N. L., 1969: The inverted 'V' cloud pattern—An easterly wave? *Mon. Wea. Rev.*, **97**, 130–140.

——, 1970: On the energetics of cold lows *Preprints of Papers, Symp. Tropical Meteorology*, Honolulu. Amer. Meteor. Soc., E IV-1 to E IV-5.

Garstang, M., 1967: Sensible and latent heat exchange in low-latitude synoptic-scale systems. *Tellus*, **19**, 492–509.

Hoeber, H., 1970: Measurements in the atmospheric surface layer above the tropical Atlantic. *Weather*, **25**, 419–424.

Holton, J. R., 1971: A diagnostic model for equatorial wave disturbances: The role of vertical shear of the mean zonal wind. *J. Atmos. Sci.*, **28**, 55–64.

Krishnamurti, T. N., 1968: A calculation of percentage area covered by convective clouds from moisture convergence. *J. Appl. Meteor.*, **7**, 184–195.

——, 1969: An experiment in numerical prediction in equatorial latitudes. *Quart. J. Roy. Meteor. Soc.*, **95**, 594–620.

——, and D. Baumhefner, 1966: Structure of a tropical disturbance based on solutions of a multilevel baroclinic model. *J. Appl. Meteor.*, **5**, 396–406.

Kumburova, P. L., and F. H. Ludlam, 1966: Rainfall evaporation in thunderstorm downdraughts. *Quart. J. Roy. Meteor. Soc.*, **92**, 510–518.

Manabe, S., J. L. Holloway, Jr., and H. M. Stone, 1970: Tropical circulation in a time-integration of a global model of the atmosphere, *J. Atmos. Sci.*, **27**, 580–613.

Morrissey, J. F., and F. J. Brousaides, 1970: Temperature-induced errors in ML-476 humidity data. *J. Appl. Meteor.*, **9**, 805–808.

Nitta, T., 1970: Statistical study of tropospheric wave disturbances in the tropical Pacific region. *J. Meteor. Soc. Japan*, **48**, 47–60.

Ooyama, K., 1969: Numerical simulation of the life cycle of tropical cyclones. *J. Atmos. Sci.*, **26**, 3–40.

Palmer, C. P., 1952: Tropical meteorology. *Quart. J. Roy. Meteor. Soc.*, **78**, 126–163.

Riehl, H., 1945: Waves in the easterlies and the polar front in the tropics. Misc. Rept. No. 17, Dept. of Meteorology, University of Chicago, 79 pp.

——, 1954: *Tropical Meteorology*. New York, McGraw–Hill, 392 pp.

——, 1965: Varying structure of waves in the easterlies. *Proc. Intern. Symp. on Dynamics of Large-Scale Processes*. Moscow, 411–416.

——, 1969: Some aspects of cumulonimbus convection in relation to tropical weather disturbances. *Bull. Amer. Meteor. Soc.*, **50**, 587–595.

——, and J. S. Malkus, 1958: On the heat balance in the equatorial trough zone. *Geophysica*, **6**, 503–538.

——, and R. P. Pearce, 1968: Studies on the interaction between synoptic and mesoscale weather elements in the tropics. Paper No. 126, Dept. Atmospheric Science, Colorado State University.

Roll, H. U., 1965: *Physics of the Marine Atmosphere*. New York, Academic Press, 426 pp.

Wallace, J. M., 1971: Spectral studies of tropospheric wave disturbances in the tropical western Pacific. *Rev. Geophys.*, **9** (in press).

——, and C.-P. Chang, 1969: Spectrum analysis of large-scale wave disturbances in the tropical lower troposphere. *J. Atmos. Sci.*, **26**, 1010–1025.

Williams, K. T., 1970: Characteristics of the wind, thermal, and moisture fields surrounding the satellite-observed mesoscale trade wind cloud clusters in the Western North Pacific. *Preprints of Papers, Symp. Tropical Meteorology*, Honolulu, Amer. Meteor. Soc., D IV-1 to D IV-6.

Yanai, M., 1961: A detailed analysis of typhoon formation. *J. Meteor. Soc. Japan*, **39**, 187–214.

——, 1963: A preliminary survey of large-scale disturbances over the tropical Pacific region. *Geofis. Intern. (Mexico)*, **3**, 73–84.

——, 1968: Evolution of a tropical disturbance in the Caribbean Sea region. *J. Meteor. Soc. Japan*, **46**, 85–109.

——, and T. Nitta, 1967: Computation of vertical motion and vorticity budget in a Caribbean easterly wave. *J. Meteor. Soc. Japan*, **45**, 444–466.

——, T. Maruyama and Y. Hayashi, 1968: Power spectra of large-scale disturbances over the tropical Pacific. *J. Meteor. Soc. Japan*, **46**, 308–323.

Zipser, E. J., 1969: The role of organized unsaturated convective downdrafts in the structure and rapid decay of an equatorial disturbance. *J. Appl. Meteor.*, **8**, 799–814.